Indian Journal of Pure & Applied Physics
Vol. 62, January 2024, pp. 9-18
DOI: 10.56042/ijpap.v62i1.5932

Enhanced Luminescence and Photocatalytic Activity of the Monovalent Sodium (Na^+) co-doped $MgAl_2O_4$:Eu^{3+} Nanostructures

Mohd Faizan[a], M Naseem Siddique[b]* & Sachin Kumar[b]

[a]Department of Physics, Mirza Ghalib College, Gaya, Bihar 823 001, India
[b]Department of Physics, A.S (PG) College Mawana, Meerut 250 401, India

Received 2 October 2023; accepted 4 December 2023

In the present work, monovalent sodium (Na^+) co-doped $MgAl_2O_4$:Eu^{3+} photocatalyst was prepared bya combustion method followed by annealing at 1000 °C. The doping of trivalent Eu^{3+} ions into a host $MgAl_2O_4$ with divalent cations leads to luminescence quenching and hence needs charge compensation to control the quenching, which was systematically studied by powder X-ray diffraction (PXRD), diffuse reflectance spectroscopy (DRS), photoluminescence (PL) and X-ray photoelectron spectroscopy (XPS) *etc*. The PL spectra of doped and co-doped samples exhibit sharp peaks around 580, 592, 611, 628 and 692 nm associated to the $^5D_0 \rightarrow {}^7F_j$ (j = 1–4) transitions of the Eu^{3+} ions, respectively. The interplay of Na^+ and Eu^{3+} ions in the host $MgAl_2O_4$ lattice appears to be an effective charge compensation mechanism that achieve better crystal quality and enhanced red luminescence of such co-doped particles. In addition, we studied the photocatalytic activity of all the prepared photocatalysts. Specifically, Na^+ co-doped $MgAl_2O_4$: Eu^{3+} photocatalyst revealed the enhanced photocatalytic activity with photodegradation efficiency 82% under visible light irradiation.

Keywords: Luminescence; Photocatalytic activity; Diffuse reflectance spectroscopy; XPS

1 Introduction

Many researchers or scientists have been attracted towards the environment-friendly and visible light driven photocatalyst for wastewater treatment. In this regard, spinel-type oxides such as $NiFe_2O_4$[1], $BaCr_2O_4$[2], $ZnGa_2O_4$[3], $CaBi_2O_4$[4] have been used as semiconductor photocatalysts with narrow band gap and efficient in the degradation of pollutants. Besides these spinel magnesium aluminates, $MgAl_2O_4$ has a great interest due to its outstanding physicochemical properties, good efficiency and high brightness, which might be used photoelectric devices, lightweight helmets, dielectric capacitors, and high temperature windows, *etc*.[5-7]. The survey for efficient and cost effective photocatalysts is still trending. In recent, a lot of works is still continuing to develop effective photocatalytic under a visible light. $MgAl_2O_4$ exhibits unique physical properties like cubic spinel AB_2O_4 structure (cubic spinel, Fd-3m)[8] and a wide band gap energy ~5.0 eV[9,10]. Several researchers[11-13] have already studied the transition metal ions (Cr^{3+}, Ni^{2+}, Mn^{2+}, *etc*.) doped spinel crystal ($MgAl_2O_4$). Nevertheless, rare earth (RE) dopants related luminescent materials have been extensively used in optical fields including electroluminescent devices and lasers[14]. Among different RE dopants, europium ion (Eu^{3+}) doped materials have widely synthesized and their outstanding optical properties have been studied[15-17]. In general, an effective optical phenomenon occurred via the transfer of energy from the host material to the RE ions. Among different RE ions, the typical d-f transition of Eu^{3+} demonstrated many potential applications in the solid-state lighting devices. The host material having wide band gap energy can extensively transfer from host to RE ions and therefore, not only RE ions but the host material is also essential criterion to achieve improved luminescence. Several researchers[18-22] have been synthesized $MgAl_2O_4$ nanoparticles by different techniques such wet-chemical process, co-precipitation method, sol–gel method, hydrothermal route and template method etc. Though, herein we demonstrate combustion method due to several advantages like high purity, low agglomeration, simple experimental setup and short reaction time etc. It was noticed that beyond the optimum concentration, RE ions produce a luminescence quenching as the intensity of the doped nanoparticles changes as a function of concentration of the Eu^{3+} ions[23,24] The substitution of Eu^{3+} ions into $MgAl_2O_4$

*Corresponding author: (E-mail: mohdnas201@gmail.com)

lattice creates Mg vacancies which lead to decreased luminescence intensity via luminescence quenching. To overcome the quenching problem, the need of co-doping of alkali metal ions (like Li^+, Na^+) occurred as an effective way to enhance the PL intensity. Therefore, through the charge compensation mechanism, alkali metal ions not only improve the luminescence efficiency of RE ions, but they are also responsible for the good crystal quality due to reduced defects[25,26]. The charge compensation mechanism has already been carried out by Yang *et al*.[27] and Chen *et al*.[28] on the systems such as $CaWO_4:Eu^{3+}$ and $YVO_4:Eu^{3+}$, respectively and further, they revealed remarkable luminescence characteristics.

In the present work, we have reported the enhanced red luminescence via the charge compensation in such system synthesized by combustion technique annealed at 1000 ℃. The obtained nanoparticles were also characterized by using XRD, SEM, FTIR, DRS, PL and XPS. In continuation, the photocatalytic degradation of the Acid Navy Blue (ANB) dye on the co-doped magnesium aluminate spinel nanoparticles has discussed under visible light. The photocatalytic mechanism of prepared $MgAl_2O_4$ nanoparticles is interpreted in this work.

2 Experimental

The pure and co-doped $MgAl_2O_4$nanoparticles were synthesized via combustion method. In the synthesis process, the starting materials; Mg $(NO_3)_2.6H_2O$(99%), Al $(NO_3)_3.9H_2O$ (99%), $NaCO_3$, Eu_2O_3(Sigma Aldrich 99.99%) and urea (high purity) (NH_2CONH_2) as fuel agent were used. The stoichiometric amounts of oxidizer (O) and fuel (F) were taken based on the condition that the valance of F/O to be unity, using total oxidizing and reducing valences of the oxidizer and the fuel. The balance between valencies of the fuel and oxidant is significant to do the stoichiometric calculation of the mixture, which will subsequently result in improvement of maximum energy for reaction. The amount of oxidizers and fuel were calculated according to stoichiometry calculation as referred Baburao *et al*.[29]. The calculated stoichiometric amount of Mg $(NO_3)_2.6H_2O$, Al $(NO_3)_3.6H_2O$ (Al: Mg molar ratio of 2:1) and NH_2CONH_2 fuel were dissolved in 15 mL double distilled water and mixed thoroughly using magnetic stirrer for about 5-6 minutes. Further, the prepared solutions of dopants in the form of Eu_2O_3(1 mol %) and $NaCO_3$ (2 mol %) were added to get homogeneous solution. Finally, homogeneous transparent solution stirred vigorously for 30 minutes at temperature 70 °C. The transparent solution of regents was transferred into alumina crucible which was placed in a muffle furnace maintained at 550 °C. After few minutes, the solution becomes foamed and the flame was produced which lasted in 2-3 minutes. The crucible was removed from the muffle furnace and cooled at room temperature. To obtain co-doped (Eu^{3+}, Na^+) doped $MgAl_2O_4$ nanoparticles, the acquired powder was ground in a mortar and annealed at 1000 °C for 5 hours in a furnace.

The phase purity and crystalline nature of the synthesized nanomaterials were characterized by X-ray diffractometer (Rigaku Miniflex II) using Cu-K_α radiation source (λ=1.541Å). The surface and compositional analyses of prepared nanoparticles have been carried out using scanning electron microscope (SEM) and Fourier transform infrared spectroscopy (FTIR, Bruker Tensor 37). The oxidation states of europium ion have been carried out using X-ray photoelectron spectroscopy (XPS). Besides, the optical feature has been investigated using the diffuse reflectance (DRS) (Lambda-950 UV-Vis-NIR spectrophotometer) and photo-luminescence spectroscopy (PL, Perkin Elmer LS-55 fluorescent spectrometer) in the region 400-800 nm.

Photocatalytic study of investigated photocatalysts was carried out by monitoring the degradation of Acid Navy Blue (ANB) dye in a photocatalytic reactor made of glass consisting of triple jacket, UV light and an oxygen pump for the supply of oxygen to the sample. A fixed amount of 300 ml of aqueous solution of dye with 0.3g of photocatalyst were taken into the reactor. The whole mixture was stirred for 20 min in absence of UV light to approach the adsorption-desorption equilibrium. Thereafter the samples were taken out of the reactor at regular interval of time under irradiation. The concentration of degraded aliquots was calculated by measuring the absorbance using UV-Visible spectrophotometer. The following formula was used to calculate the degradation efficiency of the photocatalyst[30]

$$\text{Degradation efficiency} = \frac{C_0 - C_t}{C_0} \text{x100 (\%)} \quad \text{... (1)}$$

where C_0 and C_t is the initial and the concentration at time‘t’ respectively.

3 Results and Discussion

3.1 Structural and morphological studies

The Rietveld refined X-ray diffraction (XRD) patterns of pure, Eu^{3+} doped and Na^+ co-doped $MgAl_2O_4$ samples are illustrated in Fig. 1 and all the refined parameters are presented in Table 1. It can be seen that all the diffraction peaks are indexed as (220), (311), (400), (511), (440) and (533), which are in good agreement with the ICDD PDF card no. 01-082-2424[26]. From the XRD spectra, it is noticed that there was not found any impurity peak or secondary phase, which typically confirms the successful formation of the single-phasecubic spinel structure (Fig. 3) having the space group Fd-3m. As presented in XRD spectra, all the peaks are shifted slightly towards lower 2θ values with the increasing concentrations of Eu^{3+} as well as Na^+, resulting increased value of lattice parameter as listed in Table 1. The variation in lattice parameter reveals the successful incorporation of Eu^{3+} and Na^+ into host lattice. Hence, the expansion of the unit cell caused by the substitution of smaller Mg^{2+} (0.72 *Å)* by larger Eu^{3+} (0.95*Å)* or Na^+ (1.02 *Å)*, is usually accountable for such lower angle shift[31].

In addition, the average crystallite size (*D*) of the prepared nanoparticles is calculated using Scherrer method followed by Eq.[32]:

$$D = \frac{0.89\lambda}{\beta cos\theta} \quad \ldots (2)$$

where *D* is average crystal size, *β* is full width of half maximum (FWHM) and λ wavelength of the X-ray. As presented in Table 1, it is observed that the calculated values of *D* for all the samples were found to be in the range 20-16nm. To get more insight into the line broadening of XRD peak, we also determined the lattice strain and crystallite size with the help of Williamson Hall (W-H) method which is given by the Eq.[33]:

$$\beta \cos\theta = \frac{0.89\lambda}{D} + 4\varepsilon \sin\theta \quad \ldots (3)$$

where ε is induced lattice strain in crystallite. The values of ε and *D* were determined using the slope of linear fit and reciprocal of the intercept, respectively, as shown in Figs. 2 (a-c). As presented in Table 1, it seems that the value of *D* decreases with increasing Eu^{3+}concentration and further,increases with Na^+ co-doping. Based on Vegard's law, the substitution of Na^+ increases the D as the ionic radius of Na^+ (1.02 Å) is larger than the ionic radii of Mg^{2+} (0.72 Å) and Eu^{3+} (0.95 Å)[34,35]. Also, value of ε increases gradually with increasing concentrations of Eu^{3+} and Na^+, attributing the tensile strain induced by the insertion of dopants. It is also observed that the crystallite size obtained from W-H method as well as Scherrer method follows the same trend, showing the good consistency in both of them.

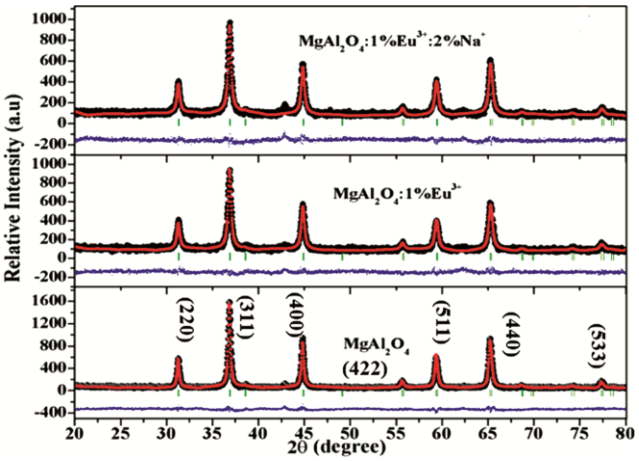

Fig. 1 — Rietveld refined XRD spectra of prepared nanoparticles.

Table 1 — Refined structural parameters for all the samples

Samples	$MgAl_2O_4$	$MgAl_2O_4:Eu^{3+}$	$MgAl_2O_4:Eu^{3+}$: Na^+
Crystal System	Cubic spinel	Cubic spinel	Cubic spinel
Space group	Fd-3m	Fd-3m	Fd-3m
a=b=c (Å)	8.0806	8.0819	8.0840
V (Å)^3	527.63	527.88	528.29
R_{Bragg}	7.90%	10.60%	14%
R_F	8.714%	7.04%	12.2%
GOF (χ^2)	2.10	1.57	1.38
Scherrer's size *D (nm)*	20.07	16.70	17.50
William's size *D(nm)*	18.90	14.33	15.45
Strain (ε x10^{-3})	0.401	0.562	0.973

The surface morphology of the prepared pure and co-doped $MgAl_2O_4$ samples was explored by scanning electron microcopy (SEM) and presented in Figs. 4(a,b). A careful examination of SEM images revealed that pure and co-doped $MgAl_2O_4$ nanoparticles are essentially aggregates of uniform spherical-shaped nanoparticles. On the other hand, the energy dispersive X-ray spectroscopy (EDX) analysis of the prepared pure and co-doped $MgAl_2O_4$ samples confirms that the molar ratio Mg:Al:O is about 1:2:4 (Figs. 4(c,d)) which indicates the stoichiometric amount of nanocrystals.

The co-ordinance state of Mg and Al cations in all the samples is confirmed by FTIR analysis. Fig. 5 shows the room temperature FTIR spectra of the

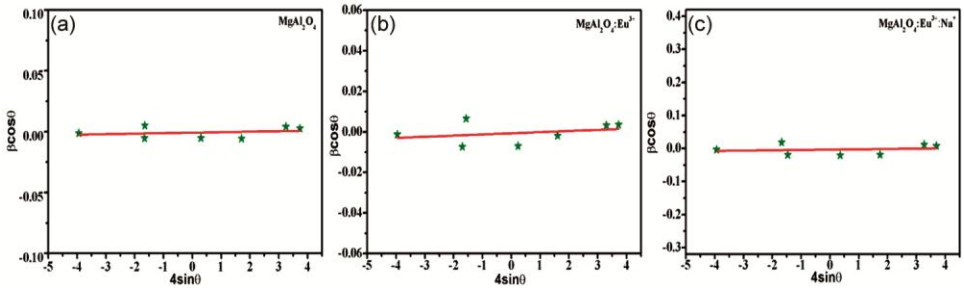

Fig 2 — W-H plots of pure (a), Eu^{3+} doped (b) and Na^{+} co-doped (c) of $MgAl_2O_4$ nanoparticles

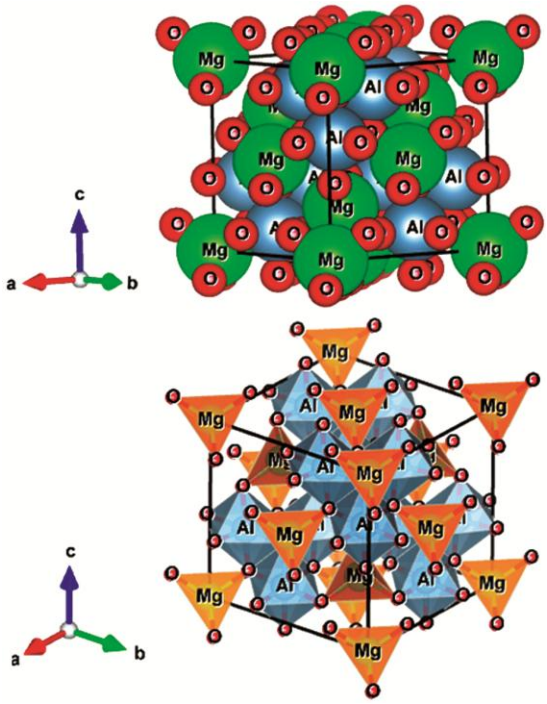

Fig 3 — Crystal structure of cubic spinel $MgAl_2O_4$ unit cell.

annealed nanoparticles prepared by combustion method, recorded in the range of 4000 - 400 cm^{-1}. It is known that the broad peaks at 3500 and 1389 cm^{-1} assigned to the OH stretching (the presence of molecular water) and bending vibration of N–O, respectively. Two more bands at (519 and 693 cm^{-1}) associated with lattice vibrations of tetra and octahedral coordinated Mg and Al metal ions, further confirmed the cubic spinel type structure of prepared materials[36].

3.2 Spectroscopic analyses

Diffuse reflectance spectroscopy (DRS) was used to study the absorption characteristics of the pure, doped and co-doped $MgAl_2O_4$ samples. Fig. 6(a) depicts the DRS spectra of prepared samples in the wavelength range of 200-800 nm. From the Fig. 6(a) (Inset), it can be seen that two absorption bands were

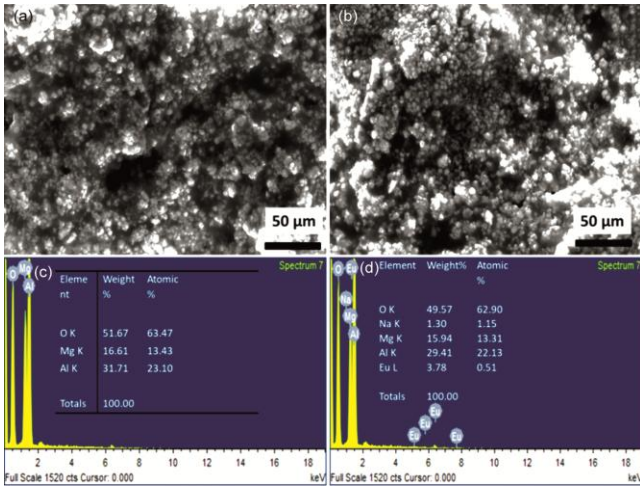

Fig 4 — (a, b) SEM images and (c, d) EDX spectra for host and co-doped $MgAl_2O_4$ samples, respectively.

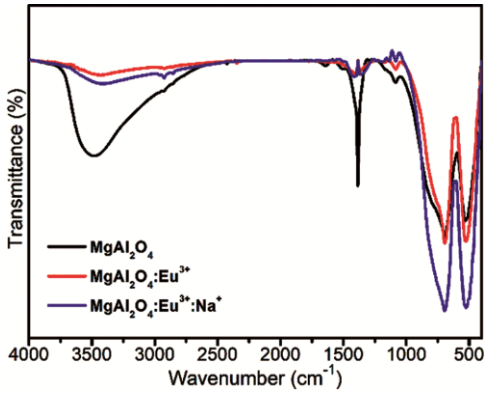

Fig 5 — FTIR spectra for all the samples.

observed in the region of 216-300 nm. The absorption band around 217 nm (5.71 eV) is attributed to the band-to-band absorption from the host material as reported in literatures[37,38]. On the other hand, the absorption band at 272 nm may be due to the intrinsic point defects within the band gap of host ($MgAl_2O_4$) material. To clear the picture, the optical band gap was also calculated from the plot of $[F(R_\infty)\ h\nu]^2$ versus $h\nu$ by extrapolating the linear fitted region at $[F(R_\infty)\ h\nu]_2=0$ which has been shown in Fig. 6(b)[39].

The estimated values of band gap energy (E_g) are found to be 4.01 eV and 3.90 eV for pure and Eu^{3+} doped samples, respectively. The value of E_g around 3.90 eV is originated from the Eu^{2+} ion (confirmed by XPS), attributed to the 4f -5d transition[40]. However, as presented in Fig. 6(b), no significant change in E_g is observed for the co- doped $MgAl_2O_4$ sample.

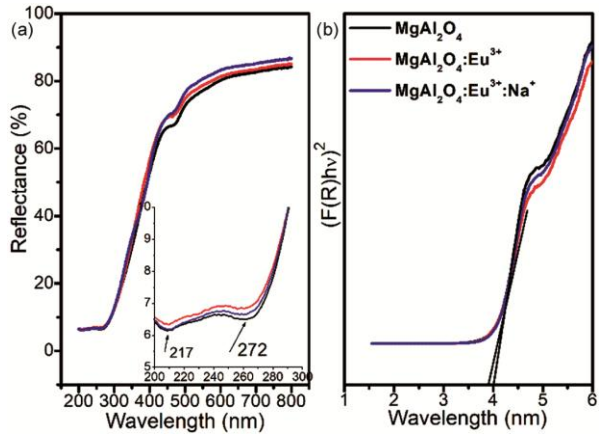

Fig 6 — (a) DRS spectra and (b) Tauc's plots for all the samples.

The photoluminescence (PL) features of the $MgAl_2O_4:Eu^{3+}$ and Na^+ co-doped $MgAl_2O_4:Eu^{3+}$ nanoparticles were explored by PL emission spectra, recorded in the wavelength range of 500-700 nm, presented in Figs. 7(a,b). To determine the peak fitting parameters, we were deconvoluted the room temperature PL emission spectra of the prepared nanoparticles, excited by 305 nm wavelength, are shown in Fig. 8(a). The extracted peak fitting parameters are presented in Table 2.

In addition, the europium oxidation states (+2 and +3) have also been confirmed by the high resolution XPS spectrum of europium ion as presented in Fig. 8(b). The XPS spectrum shows Eu $3d_{5/2}$ signals centered at 1129 and 1139 eV, revealing the +2 and +3 oxidation states of europium ion, respectively[41]. As presented in Fig. 8(a), the emission spectra of both

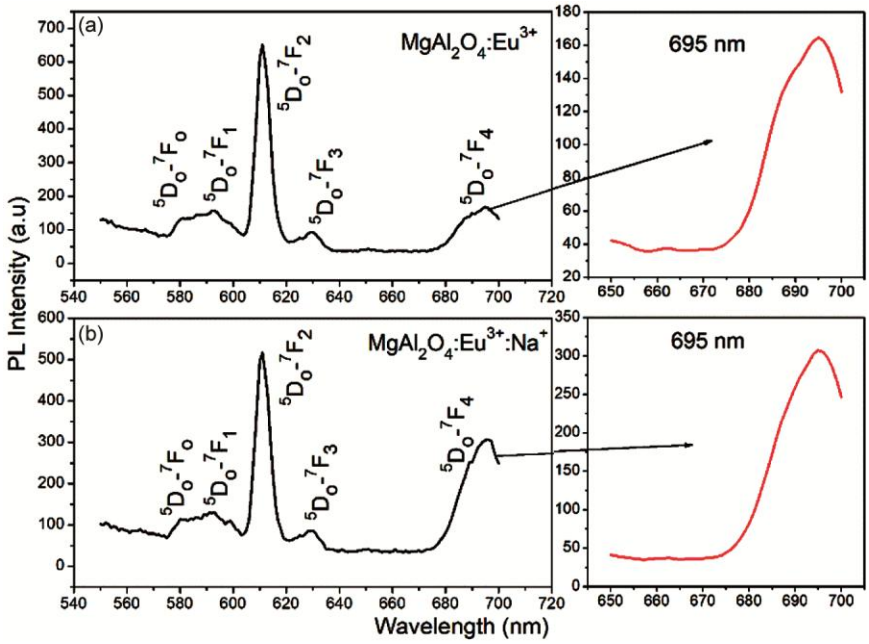

Fig 7 — (a): Photoluminescence spectra for pure and (b) co-doped $MgAl_2O_4$ samples.

Table 2 — Extracted peak fitting parameters from the deconvoluted fluorescence spectra of the doped and co-doped $MgAl_2O_4$ samples

Sample	Peak	Transition ^5D_o-^7F_o	^5D_o-$^7F_1$	^5D_o-$^7F_2$	^5D_o-$^7F_3$	^5D_o-$^7F_4$
$MgAl_2O_4:Eu^{3+}$	Center	581.91	592.04	611.23	629.55	694.52
	Area	353.45	848.61	3640.56	299.33	773.51
	FWHM	7.68	11.59	5.93	6.91	12.80
$MgAl_2O_4:Eu^{3+}$: Na^+	Center	580.94	591.63	611.13	628.89	694.59
	Area	303.36	745.29	2887.97	286.28	1439.74
	FWHM	7.70	12.51	6.04	7.59	12.27

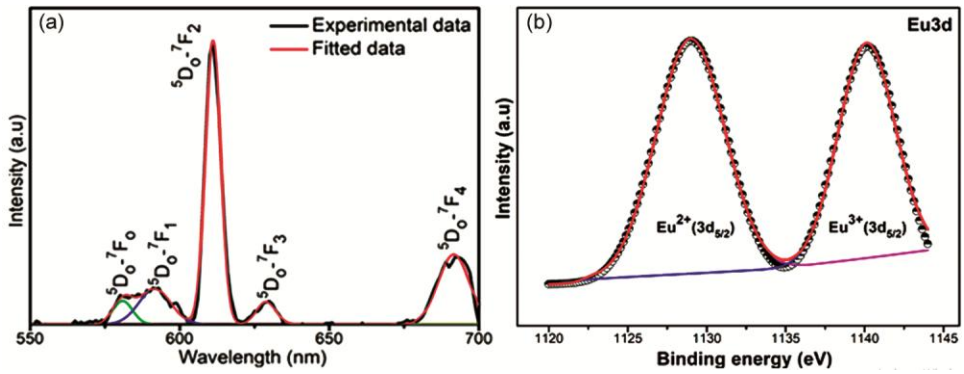

Fig 8 — (a): Deconvoluted PL spectrum of Na^+ co-doped $MgAl_2O_4$:Eu^{3+} and (b) XPS spectrum of Eu^{3+} ion.

the Eu^{3+} doped and Na^+ co-doped samples principally consist of sharp and intense lines ranging from 580 to 700 nm. In general, it is seen that Eu^{3+} replaces Mg^{2+} in $MgAl_2O_4$ hence, Eu^{3+} occupies tetrahedral positions with 8a symmetry (according to Wyckoff notation). In such configuration, four O^{2-} provide the crystal field which further splits the energy levels of Eu^{3+}. As presented in Fig. 8(a) and Table 2, the five peaks observed around 580, 592, 611, 628 and 692 nm are ascribed to the $^5D_0 \rightarrow {}^7F_j (j = 1–4)$ transitions of the Eu^{3+} ions, respectively. Usually, $^5D_0 \rightarrow {}^7F_1$ and $^5D_0 \rightarrow {}^7F_2$ lines originate from magnetic and electric dipole transitions, respectively. The magnetic dipole transition does not depend on symmetry as well as the site occupied by Eu^{3+} ions in the host. Though, the electric dipole transition is hypersensitive, and hence, the symmetry of the host lattice typically affects the emission intensity. Since for both the doped and Na^+ co-doped $MgAl_2O_4$ samples, non-inversion symmetric Mg^{2+} sites occupied by Eu^{3+} ions, electric dipole transitions dominate and associated peak around 611 nm is the most intense for doped and co-doped samples. Fig. 9 displays the schematic energy level diagram of Eu^{3+} ions and designates essential transitions related to luminescence mechanism of doped sample.

As seen in Fig. 8(a), there is observed a red emission in trivalent Eu^{3+} doped sample which further enhanced by the co-doping of monovalent Na^+ in $MgAl_2O_4$:Eu^{3+}. This result can be explained as: the charge imbalance created in the system by the doping of trivalent ion Eu^{3+} that substitutes the divalent ion (Mg^{2+} here), resulting formation of point defects or vacancies in the $MgAl_2O_4$ lattice. In general, these defects play a role as luminescence quenchers and hence, to overcome the quenching in material, different alkali metals can be used for charge

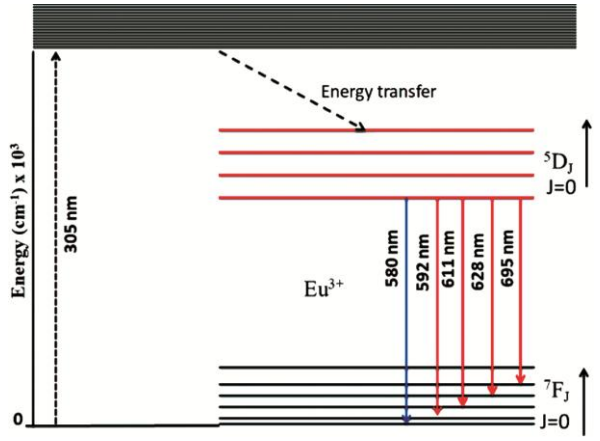

Fig 9 — Schematic energy level diagram with the emission mechanism in Eu^{3+} doped $MgAl_2O_4$.

compensation in Eu^{3+} doped $MgAl_2O_4$ phosphors. Hence, one can reduce the quenching via charge compensation by the co-doping of monovalent positive ions in such doped systems. Therefore, the reduced quenching via charge compensation can improve the emission intensity of such doped systems. In the present work, the enhancement in red emission achieved by charge compensation through the substitution of divalent Mg^{2+} ion by a trivalent Eu^{3+} and a monovalent Na^+ ion (Fig. 8(a)). However, it is not observed any significant change in the emission wavelengths (PL peak positions) with the Na^+ concentration, while the red emission is prominently increased by the Na^+ co-doping compared to Eu^{3+} doped $MgAl_2O_4$ sample. The better red emission (~ 695 nm) of co-doped sample further confirmed by the increased value of peak area as presented in Fig. 10(a) and Table 2.

Through the electrically neutrality in the lattice, several Mg^{2+} vacancies (V''_{Mg}) are produced via substituting the three Mg^{2+} ions by two Eu^{3+} ions given by the equation as:

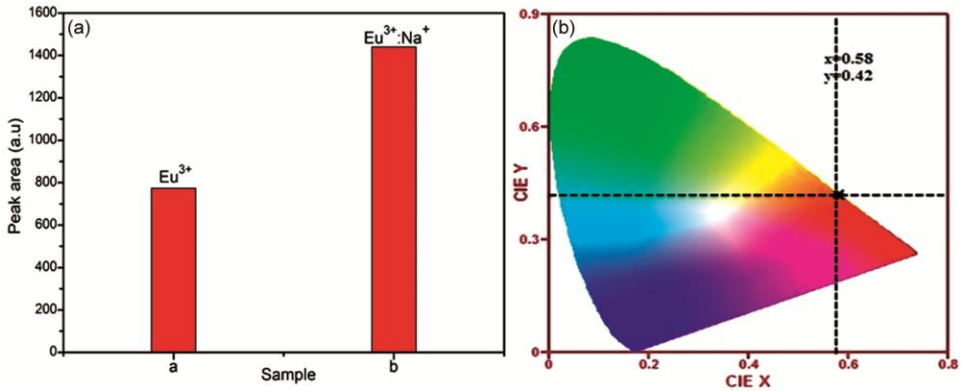

Fig 10 — (a): Variation in PL peak area for doped and co-doped and (b) CIE chromaticity co-ordinates for Na^+ co-doped $MgAl_2O_4$ sample.

$$3Mg_{Mg} \rightarrow 2Eu_{Mg} + V_{Mg}^{"} \quad \ldots (4)$$

Thus, these formed Mg^{2+} vacancies ($V_{Mg}^{"}$) act as lattice defects which responsible for the luminescence quenching, caused by further energy transfer from luminescence centers to the defect sites[42]. In general, the luminescence quenching occurs due to nonradiative energy transfer, which takesplace as a result of an exchange interaction, or a multipole–multipole interaction. In the complex electric multipolar interaction for the energy transfer, there are diverse types of interactions, such as dipole–dipole (d–d), dipole–quadrupole (d–q), quadrupole–quadrupole (q–q) interactions, *etc*. Overall, the most common interaction in the concentration quenching transition of metal oxide nanomaterials is the d–d interaction[43-45].

Therefore, to achieve the charge balance, one can add the alkali metal ions (Na^+) along with the rare earth activators (Eu^{3+}). The incorporation of Na^+ ion decreases the probability of nonradiative transition and significantly increases the intensity of PL emission as given by the following equation:

$$2V_{Mg}^{"} + Eu^{3+} + Na^{+} \rightarrow Eu_{Mg} + Na_{Mg}^{'} \quad \ldots (5)$$

The charge compensation by the Na^+ ions also leads to reduced defects or vacancies, revealing a improved crystal quality as well as luminescence of Na^+ co-doped sample[46]. To clear the picture, we have also given the pictorial representation of strategy of improved red emission via charge compensation as displayed in Fig. 11. On the other hand, the emitted color in Na^+ co-doped $MgAl_2O_4:Eu^{3+}$ is displayed in CIE 1931(Commission Internationale de I'Eclairage, 1931) chromaticity diagram (Fig. 10(b)). The CIE coordinate was determined with the help of a color

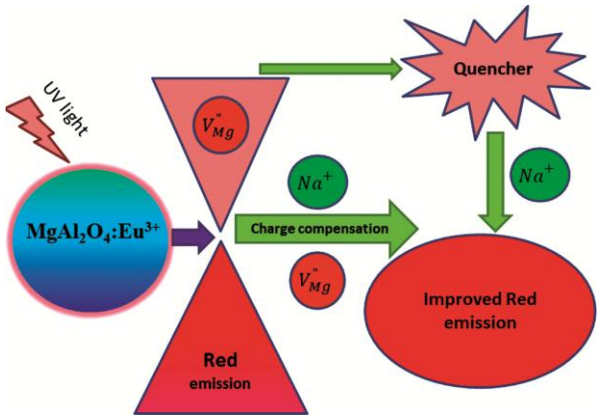

Fig 11 — Pictorial representation of improved red emission via charge compensation.

calculator program. The color co-ordinates for Na^+ co-doped $MgAl_2O_4:Eu^{3+}$ found to be (0.58, 0.42); revealing red emission in co-doped system. Consequently, the produced red emission of the prepared nanoparticles intensely suggests that such material might be used for the fabrication of solid-state lighting devices.

3.3 Photocatalytic activity

The photocatalytic activity of $MgAl_2O_4$ was determined by monitoring the degradation of aqueous solution of ANB dye (λmax 560 nm) in presence of UV light. The photodegradation process was checked by measuring the absorbance of the degraded samples of dye using UV-visible spectroscopy. To discuss the efficiency of the prepared samples for the degradation of ANB dye, each sample was tested as a function of irradiation time. Fig. 12 demonstrates degradation of ANB dye under UV-irradiation at different reaction times from 20 to 90 minutes where the intensity of absorption peak decreases with increasing irradiation under visible light. The continuous decline in the

absorbance of the aliquots indicates the degradation of the ANB dye molecules.

The degradation efficiency and equivalent percentage of pure and co-doped $MgAl_2O_4$ were determined by estimating the change in the concentration of ANB dye as a function of irradiation time, as shown in Fig. 13(b). The values of degradation percentage of the ANB dye by $MgAl_2O_4$, $MgAl_2O_4$:Eu^{3+} and Na^+ co-doped $MgAl_2O_4$:Eu^{3+} after sunlight irradiation for 90 min were 64%, 69% and 82%, respectively. This excellent result is ascribed to the Na^+ co-doped $MgAl_2O_4$:Eu^{3+} (Z) with 82 % photodegradation of ANB dye after sunlight irradiation for 90 minutes that revealed the reduced recombination of electron−hole pairs. The controlled recombination of electron−hole pairs leads to the enhanced light harvesting ability and further, stimulates the photoactivity of the catalyst[47,48]. On the other hand, the decreased photocatalytic activity revealedby $MgAl_2O_4$ (X), $MgAl_2O_4$:Eu^{3+} (Y) with degradation efficiency 64 % and 69 %, ascribed to thelow electrical conductivity. Moreover, the photocatalytic degradation efficiency of semi-conductors catalysts depends on the numerous characteristics (crystal structure, crystallite size, surface area, band gap and surface defects).

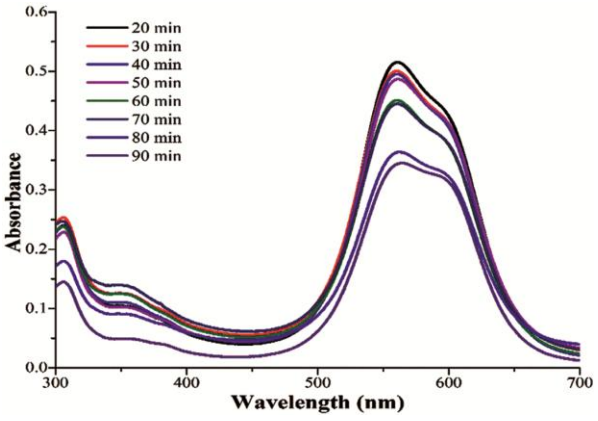

Fig 12 — UV-Visible spectra of the photodegraded samples of ANB dye.

3.3.1 Mechanism of photocatalytic activity

The photocatalytic activity of the $MgAl_2O_4$ catalyst studied under the visible light for the photodegradation of the ANB dye. The probable mechanism of the photocatalytic degradation of the ANB dye in presence of $MgAl_2O_4$ is shown in Fig. 14. Upon the irradiation of UV light to $MgAl_2O_4$, electrons from the Valence band (VB) drift to the Conduction Band (CB). Further, the photogenerated electrons in the CB reduced O_2 molecules to $\cdot O_2^-$ radicals mean while photogenerated h^+ in the VB of the $MgAl_2O_4$ oxidize the H_2O molecules to ·OH radicals. The VB potential of the $MgAl_2O_4$ is sufficient to oxidize the H_2O molecules. Thus the $\cdot O_2^-$ and ·OH radicals formed in the mechanism will

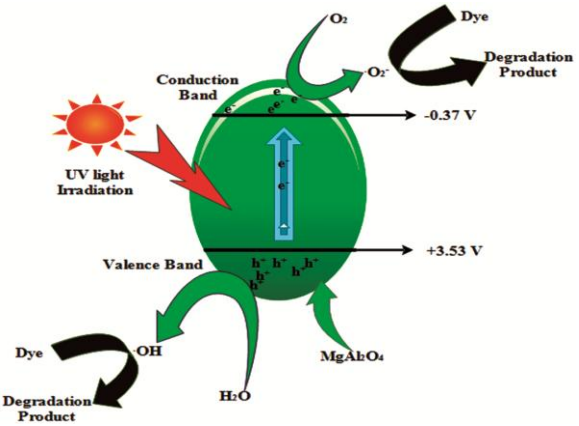

Fig 14 — Possible photocatalytic mechanism of the $MgAl_2O_4$ for the degradation of ANB dye.

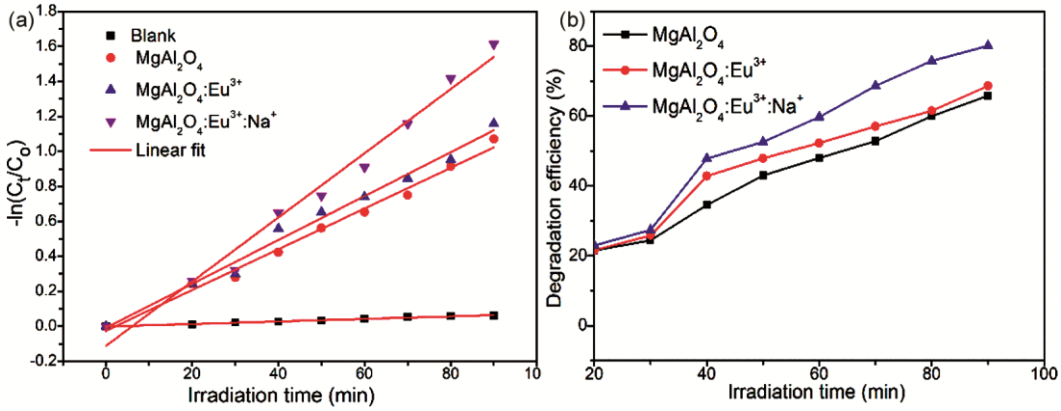

Fig 13 — (a) Calculation of pseudo-first order rate constants of ANB dye and (b) Percentage degradation efficiency of ANB dye in the presence of as-prepared catalysts.

Table 3 — Extracted Pseudo-first order rate constants of ANB dye in the presence of prepared samples

Sample	Pollutant	Rate constant (k)min^{-1}
$MgAl_2O_4$	ANB Dye	0.011
$MgAl_2O_4:Eu^{3+}$	ANB Dye	0.013
Na^+ co-doped $MgAl_2O^4:Eu^{3+}$	ANB Dye	0.021

interact to ANB molecules leads to degradation into the simpler product.

The following proposed reaction occurs in the degradation of ANB dye:

$$MgAl_2O_4 + h\nu \rightarrow MgAl_2O_4\ (e^-/h+) \quad \text{... (6)}$$

$$(e^-) + O_2 \rightarrow \dot{O}_2^- \quad \text{... (7)}$$

$$h^+ + H_2O \rightarrow \cdot OH \quad \text{... (8)}$$

$$O_2^-/h+/e^-/\dot{O}H + \text{ANB dye} \rightarrow \text{Degradation Product} \quad \text{... (9)}$$

3.3.2 Kinetic study of photocatalysis

The kinetic study of ANB dye has been analyzed on the basis of Langmuir- Hinshelwood model by determining the reaction order of ANB dye, which is given as[49]

$$r = \frac{dC}{dt} \quad \text{... (10)}$$

The photodegradation reactions for ANB monitor follows the pseudo-first order kinetics, and further, the rate constants (k) of the catalytic reaction are determine using the relation[50]:

$$Ln\left(\frac{C}{C_o}\right) = -k \quad \text{... (11)}$$

where (t) is the time of sunlight irradiation.

As presented in Table 3, the photocatalytic degradation of ANB by the Na^+ co-doped $MgAl_2O^4:Eu^{3+}$ photocatalyst reveals the fastest kinetics with a rate constant of 0.021 min^{-1}, which is significantly higher than the degradations by the $MgAl_2O_4$(k = 0.011 min^{-1}), and $MgAl_2O_4:Eu^{3+}$ (k = 0.013 min^{-1}) photocatalysts. This result demonstrates that the co-doping of Na inhibited the recombination probability of the excited charge carrier in $MgAl_2O_4$ which further leads to the enhanced photocatalytic efficiency.

4 Conclusion

In this work, the host and co-doped (Eu^{3+}, Na^+) $MgAl_2O_4$ photocatalyst have been synthesized by a combustion method annealed at 1000 ℃ The powder XRD and Rietveld refinement studies of the nanoparticles confirmed the successful formation of the single-phasecubic spinel structure having the space group Fd-3m. The average crystal size of the pure, Eu^{3+}doped and Na^+ co-doped of $MgAl_2O_4$ nanoparticles were calculated using both Scherrer and W-H methods in the range 16-20 nm and 14- 18 nm, respectively. The surface morphology and compositional analyses of prepared nanoparticles (NPs) have also been studied using the SEM and FTIR spectroscopy, revealing the spinel type structured highly agglomerated spherical-shaped nanoparticles. In addition, the absorption characteristics of the prepared NPs have also been studied using the DRS in the wavelength range of 200-800 nm. The DRS spectra exhibited two absorption bands in the region of 216-300 nm, confirming the optical band gap energy lie in the range 3.90-4.10 eV. On the other hand, the Eu oxidation states have also been confirmed by the high resolution XPS spectrum of europium ion. The XPS spectrum showed Eu $3d_{5/2}$ signals centered at 1129 and 1139 eV, revealing the +2 and +3 oxidation states of europium ion, respectively. To discuss the luminescence behavior of doped and co-doped samples, photoluminescence (PL) spectra (excited by 305 nm) have been recorded in the wavelength range of 500-700 nm. The deconvoluted room temperature PL emission spectra of the prepared doped and co-doped nanoparticles showed five peaks observed around 580, 592, 611, 628 and 692 nm ascribed to the $^5D_0 \rightarrow {}^7F_j$(j = 1–4) transitions of the Eu^{3+} ions, respectively. The transitions $^5D_0 \rightarrow {}^7F_1$ and $^5D_0 \rightarrow {}^7F_2$ typically originate from magnetic and electric dipole transitions, respectively. As seen in PL spectra, a red emission (~695 nm) was observed in trivalent Eu^{3+} doped sample which further enhanced by the co-doping of monovalent Na^+ in $MgAl_2O_4:Eu^{3+}$. Although, red emission in Na^+ co-doped $MgAl_2O_4:Eu^{3+}$ was confirmed by the associated CIE color coordinate (0.58, 0.42). The enhanced PL red emission can be explained via charge compensation by the Na^+ ions which also provide better crystal quality. The incorporation of Na^+ ion reduces luminescence quenching and hence, considerably increases the intensity of red emission. Consequently, the improved red emission of the prepared nanoparticles intensely suggests that such material might be used for the fabrication of solid-state lighting devices. In continuation, the photocatalytic activity has also been discussed of prepared photocatalysts. Among this series of photocatalyst,

Na^+ co-doped $MgAl_2O_4:Eu^{3+}$photocatalyst exhibited good photocatalytic activity and the photodegradation rate for ANB dye achieved 82% under visible light irradiation. We concluded that the enhanced photocatalytic ability was attributed to the monovalent Na^+ co-doping content, which control the electron-hole recombination centers and further created more photoactive sites. For co-doped photocatalyst, the photocatalytic degradation process followed pseudo first order law with rate constant 0.021 min^{-1} for the visible light.

Acknowledgments

Authors are very grateful to Prof. Shabbir Ahmed Department of Physics Aligarh Muslim University, Aligarh (India) for providing experimental facilities.

Conflicts of interest

The authors declare no competing financial interests**.**

References

1 Zhu Z R, Li X Y, Zhao Q D, Li H, Shen Y & Chen G H, *Chem Eng J*, 165 (2010) 64.
2 Wang D F, Zou Z G & Ye J H, *Chem Phys Lett*, 373 (2003) 191.
3 Boppana V B R, Doren D J & Lobo R F, *Chemsuschem*, 3 (2010) 814.
4 Tang J W, Zou Z G & Ye J H, *Angew Chem Int Ed*, 43 (2004) 4463.
5 Takebuchi Y, Fukushima H, Nakauchi D, Kato T, Kawaguchi N & Yanagida T, *J Lumin*, 223 (2020) 117139.
6 Choi J, Tseng T K, Davidson M & Holloway P H, *J Mater Chem*, 21 (2011) 3113.
7 Du F, Zhu R, Huang Y, Tao Y & Seo H J, *Dalton Trans*, 40 (2011) 11433.
8 Singh V, Haque M D M & Kim D-K, *Bull Korean Chem Soc*, 28 (2007) 2477.
9 Sampath S K, Kanhere D G & Pandey R, *J Phys Condens Matter*, 11 (1999) 3635.
10 Paiva R, Carvalhaes M & Blak A R, *Phys Stat Sol*, 4 (2007) 1238.
11 Kuleshov N V, Shcherbitsky V G, Mikhailov V P, Kuck S, Koetke J, Petermann K & Huber G, *J Lumin*, 71 (1997) 265.
12 Rossi F, Pucker G, Montagna M, Ferrari M & Boukenter A, *Opt Mater*, 13 (2000) 373.
13 Singh V, Chakradhar R P S, Rao J L & Kim D K, *J Solid State Chem*, 180 (2007) 2607.
14 Hoppe H A, *Angew Chem Int Ed*, 48 (2009) 3572.
15 Siddique M N, Faizan Md, Riyajuddin S, Tripathi P & Ahmad S, *J Alloys Compd*, 850 (2021) 156748.
16 Ghosh K, Liang H, Zhang Q, Zheng Z Q, Ming H, Li Z C, Xu J, Chen B & Zhao H, *Opt Lett*, 29 (2004) 477.
17 Ishizaka T & Kurokawa Y, *J Appl Phys*, 90 (2001) 243.
18 Li J G, Ikegami T, Lee J H, Mori T & Yajima Y, *Ceram Int*, 27 (2001) 481.
19 Zawrah M F, Hamaad H & Meky S, *Ceram Int*, 33 (2007) 969.
20 Saberi A, Golestani-Fard F, Willert-Porada M, Negahdari Z, Liebscher C & Gossler B, *Ceram Int*, 35 (2009) 933.
21 Zhang X, *Mater Chem Phys*, 116 (2009) 415.
22 Hashimoton S, Honda S, Hiramatsu T & Iwamoto Y, *Ceram Int*, 139 (2013) 2077.
23 Geng D, Shang M, Yang D, Zhang Y, Cheng Z & Lin J, *Dalton Trans*, 41 (2012) 14042.
24 Geng D, Li G, Shang M, Peng C, Zhang Y, Cheng Z & Lin J, *Dalton Trans*, 41 (2012) 3078.
25 Yang H K, Choi H, Moon B K, Choi B C, Jeong J H, Kim J H & Kim K H, *Solid State Sci*, 12 (2010) 1445.
26 Saha Subhajit, Das Swati, Ghorai U K, *et al*., *Dalton Trans*, 42 (2013) 12965.
27 Yang H K, Choi H, Moon B K, Choi B C, Jeong J H, Kim J H & Kim K H, *Solid State Sci*, 12 (2010) 1445.
28 Chen Y, Yang H K, Park S W, Moon B K, Choi B C, Jeong J H & Kim K H, *J Alloys Compd*, 511 (2012) 123.
29 Sherikar B N & Umarji A M, *Trans Indian Ceram Soc*, 70 (2011) 167.
30 Siddique M N, Ahmad N & Tripathi P, *Opt Mater*, 107 (2020) 110101.
31 Han J Y, Im W B, Lee G Y & Jeon D Y, *J Mater Chem*, 22 (2012) 8793.
32 Siddique M N, Ahmed A, Riyajuddin S K, Faizan Md, Ghosh K & Tripathi P, *J Magn Magn Mater*, 500 (2020) 166323.
33 Siddique M N & Tripathi P, *J Alloys Compd*, 825 (2020) 154071.
34 Naik R, *et al*., *Sens Actuators B*, 195 (2014) 140.
35 Qian S, et al., *Mater Res Bull*, 48 (2013) 521.
36 Waldner K F, Laine R M, Dhumrongvaraporn S, Tayaniphan S & Narayanan R, *Chem Mater*, 8 (1996) 2850.
37 Paiva R, Carvalhaes M & Blak A R, *Phys Stat Sol C*, 4 (2007) 1238.
38 Sampath S K, Kanhere D G & Pandey R, *J Phys Condens Matter*, 11 (1999) 3635.
39 Faizan Md, Siddique M N, Ahmad S, Tripathi P & Riyajuddin S, *J Alloys Compd*, 853 (2021) 157378.
40 Xia Z, Zhuang J, Liu H & Liao L, *J Phys D Appl Phys*, 45 (2012) 015302.
41 Zhao F, Sun H L, Gao S & Su G, *J Mater Chem*, 15 (2005) 4209.
42 Qiang R F, Xiao S, Ding J W, Yuan W & Zhu C, *J Lumin*, 129 (2009) 826.
43 Ashwini S, *et al.*, J Sci: Adv Mater Dev, 4 (2019) 531.
44 Naik R, *et al*., *J Lumin*, 197 (2018) 233.
45 Yoganand H S, *et al*., *J Alloys Compd*, 768 (2018) 451.
46 Ambast A K, Goutam J, Som S & Sharma S K, *Spectrochim Acta A*, 122 (2014) 93.
47 Nathir A F, Al-Rawashdeh, Allabadi O & Aljarrah M T, *ACS Omega*, 5 (2020) 28046.
48 Wan J, Jiang X, Li H, Chen K, *J Mater Chem*, 22 (2012) 13500.
49 Ahmad I, *et al*., *Separ Purif Technol*, 237 (2020) 116328.
50 Deng Q, Duan X, Ng D H L, Tang H, Yang Y, Kong M, Wu Z, Cai W & Wang G, *ACS Appl Mater Interf*, 4 (2012) 6030.